Dalton Transactions

Structural and Thermal Properties of Ultralow Thermal Conductivity Ba3Cu2Sn3Se10

Journal:	*Dalton Transactions*
Manuscript ID	DT-ART-01-2022-000309.R2
Article Type:	Paper
Date Submitted by the Author:	24-Mar-2022
Complete List of Authors:	Ojo, Oluwagbemiga; University of South Florida College of Arts & Sciences, Physics Gunatilleke, Wilarachchige ; University of South Florida College of Arts & Sciences, Physics Wang, Hsin; Oak Ridege National Lab, Materials Science and Techonology Nolas, George; University of South Florida, Department of Physics

ARTICLE

Structural and Thermal Properties of Ultralow Thermal Conductivity $Ba_3Cu_2Sn_3Se_{10}$

Received 00th January 20xx,
Accepted 00th January 20xx

DOI: 10.1039/x0xx00000x

Oluwagbemiga P. Ojo,[a] Wilarachchige D. C. B. Gunatilleke,[a] Hsin Wang,[b] George S. Nolas[a]*

The thermal properties of $Ba_3Cu_2Sn_3Se_{10}$ were investigated by measurement of the thermal conductivity and heat capacity. The chemical bonding in this diamagnetic material was investigated using structural data from Rietveld refinement and calculated electron localization. This quaternary chalcogenide is monoclinic ($P2_1/c$), has a large unit cell with 72 atoms in the primitive cell, and a high local coordination environment. The Debye temperature (162 K) and average speed of sound (1666 m/s) are relatively low with a very small electronic contribution to the heat capacity. Ultralow thermal conductivity (0.46 $Wm^{-1}K^{-1}$ at room temperature) is attributed to the relatively weak chemical bonding and intrinsic anharmonicity, in addition to a large unit cell. This work is part of the continuing effort to explore quaternary chalcogenides with intrinsically low thermal conductivity and identify the features that result in a low thermal conductivity.

Introduction

Quaternary chalcogenides continue to be investigated because of the diverse physical properties that are associated with their crystal structures. Different quaternary chalcogenides are of interest for applications in nonlinear optics [1–4], photovoltaics [5–8], thermoelectrics [9–13], and as thermal barrier coating materials [9,14,15]. Moreover, materials for applications where heat dissipation or low thermal conductivity are of interest requires an understanding of their thermal properties. Quaternary chalcogenides possess very different physical properties depending on their stoichiometry and crystal structure; therefore, the potential applications for these materials are directly related to their structural features. In particular, the thermal properties of these materials have been shown to be directly related to their specific structural features [16–20] .

One aspect that motivates the interest in these materials is their bonding and structural arrangement, in particular the coordination preferences of the metal and chalcogen atoms that comprise complex structural features that can result in anharmonicity. Many atoms per unit cell result in a large number of optic modes that typically have lower group velocities than the acoustic modes that often dominate thermal transport [21–23]. In the case of $Ba_3Cu_2Sn_3Se_{10}$, there are 72 atoms in the primitive unit cell. The complex crystal structure of this quaternary chalcogenide has been previously reported, as well as the calculated band structure which shows a large 1.2 eV bandgap [24]. Motivated by our continued interest in quaternary chalcogenides, and in particular the effect of complex structures, bonding, and disorder on the thermal properties, we investigate the temperature-dependent thermal properties of monoclinic ($P2_1/c$) $Ba_3Cu_2Sn_3Se_{10}$. Rietveld refinement and calculated electron localization are also employed in determining the origins of the thermal properties.

Experimental

Phase pure $Ba_3Cu_2Sn_3Se_{10}$ was prepared by mechanical alloying of the starting binaries in a planetary ball mill, followed by solid-state annealing. The binary Cu_2Se (99.5%, Alfa Aesar) was of commercial grade while the phase pure BaSe and $SnSe_2$ binary materials were synthesized by direct reaction of the constituent elements. BaSe was prepared by stoichiometric reaction of Ba pieces (99.2%, Alfa Aesar) and Se powder (99.999%, Alfa Aesar) at 1213 K for 3 days, and $SnSe_2$ was prepared by stoichiometric reaction of Sn powder (99.85%, Alfa Aesar) and Se mesh powder (99.999%, Alfa Aesar) at 1273 K for 12 h. Subsequently, BaSe, Cu_2Se, and $SnSe_2$ were weighed in a 3:1:3 ratio and placed into a stainless-steel milling jar together with stainless-steel balls in a ball-to-powder ratio of 40:1. The milling jar was evacuated and back-filled with Argon before sealing, and subsequently ball-milled at 425 rpm for 10 minutes. The powder product obtained from ball milling was cold pressed and placed in a resistive furnace at 773 K for 72 h. Phase pure microcrystalline $Ba_3Cu_2Sn_3Se_{10}$ was obtained as indicated from powder X-ray diffraction (XRD) measurements and Rietveld structure refinement. The short ball-milling duration (10 min) allows for homogeneous mixing followed by formation of the desired phase by reaction at moderate temperatures. This synthetic approach allowed for the formation of microcrystalline phase-

[a] Department of Physics, University of South Florida, Tampa, FL, 33620, USA.
[b] Materials Science and Technology Division, Oak Ridge National Laboratory, Oak Ridge, TN 37831, USA.
* Corresponding author: gnolas@usf.edu

pure powders in large quantities that were subsequently densified in order to perform the thermal property measurements described below. Hot pressing was used to densify the finely ground and sieved (325 mesh; 45 μm) powders. The powders were loaded into a custom-designed graphite punch-die assembly and densified at 150 MPa and 673 K for 2 h under high purity N_2 gas flow resulting in a dense polycrystalline material of 95 % of theoretical density.

Powder X-ray diffraction data was collected using a Bruker-AXS D8 Focus diffractometer in the Bragg Brentano geometry with a Cu anode and graphite monochromator (λ = 1.5406 Å). Structural refinements were carried out using GSAS II software [25]. The background was described by the Chebyshev-1 function containing ten terms, profile parameters were refined to fit the peak shapes of the XRD spectra, and a pseudo-Voigt profile function was employed for the refinement. Differential thermal analysis (DTA) and thermogravimetric analysis (TGA) measurements were performed from 300 K to 1073 K with a heating rate of 10 K/min on 20 mg powder under high purity N_2 gas flow using a TA Instruments Q600. Isobaric heat capacity, C_p , measurements in the 2 K to 300 K temperature range was performed using a commercial Quantum Design Physical Property Measurement System (PPMS), with a maximum estimated uncertainty of 5 % for the entire temperature range. DC magnetic susceptibility was measured from 10 K to 300 K using the VSM module of the Quantum Design PPMS equipped with a brass paddle in a magnetic field of 10000 Oe. Thermal diffusivity, α, was measured using a NETZSCH LFA457 system under Ar flow that employs the laser flash diffusivity method. The experimental uncertainty in α measurements was estimated to be ± 5%. The equation $\kappa = D\alpha C_p$ was used to compute the thermal conductivity, κ, where *D* is the measured density of the densified polycrystalline material and C_p is specific heat capacity.

Electron localization function (ELF) calculations were carried out based on self-consistent Kohn-Sham orbitals as implemented in the Quantum Espresso package [26] employing the structural data from our refinement results. Self-consistent field (SCF) calculations were based on the Perdew–Burke-Ernzerhof (PBE) approximation [27,28] with projector-augmented waves (PAW) pseudopotentials [29]. For the pseudopotentials, Ba $5s^25p^66s^2$, Cu $3d^{10}4s^1$, Sn $4d^{10}5s^25p^2$ and Se $4s^24p^4$ valence configurations were considered. A 2 x 2 x 1 k mesh, kinetic energy cut- off of 816 eV and energy convergence threshold of 10^{-8} eV was used. Vesta software [30] was utilized for the analyses and visualization of the ELF distribution.

Results & Discussion

Figure 1 shows the profile fit and difference from Rietveld structure refinement of the powder XRD of $Ba_3Cu_2Sn_3Se_{10}$. The results of our structure refinements are summarized in Table 1 and the atomic coordinates are given in Table 2. These results are in agreement with previously reported single crystal analyses[24]. $Ba_3Cu_2Sn_3Se_{10}$ is monoclinic, $P2_1/c$ space group, with

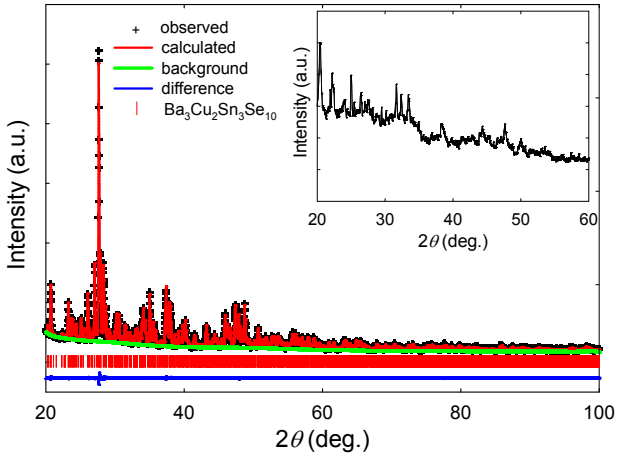

Figure 1. XRD data for $Ba_3Cu_2Sn_3Se_{10}$, including the profile fit and profile difference from Rietveld structure refinement. The inset shows XRD data after ball milling indicating that the quaternary chalcogenide was not obtained at this stage.

four formula units per unit cell and with three crystallographic Ba sites, two Cu sites, three Sn sites and ten Se sites. The crystal structure (Figure 2) can be understood as consisting of a network of interconnected polyhedra, two with eight Se atoms in a square antiprismatic arrangement with Ba1 and Ba2 at their center, Ba3 surrounded by 7 Se atoms in a monocapped trigonal prismatic geometry, slightly distorted tetrahedra with Sn1, Sn2 and Sn3 at their centers, and distorted trigonal pyramids surrounding Cu1 and Cu2. With the exception of Cu1 and Sn1, the cation-centered polyhedra are interconnected with at least one edge-sharing Se atoms and Cu1 and Sn1 polyhedra each share corners in the complex crystal structure. The larger isotropic displacement parameters, U_{iso}, for the Cu atoms suggest relatively weak bonding to Se. The distances from cation to the neighboring Se atoms vary significantly in this quaternary chalcogenide, as shown in Table 3, and range from 2.341(13) Å for Cu1-Se1 to 3.6915 (4) Å for Ba3-Se6. The associated bond angles are also given in Table 3. To understand the bonding behavior of the atomic structure, including the localization of electrons, we calculated the ELF for $Ba_3Cu_2Sn_3Se_{10}$ on different lattice planes, as shown in Figure 3. The highly localized electron density for Cu1 and Cu2 correspond to the filled *d* orbitals. Barium and Cu atoms couple with adjacent Se atoms in a primarily ionic bond while Sn-Se covalently share electrons in the structure with a mixed

Table 1. Crystallographic information and structure refinement results for $Ba_3Cu_2Sn_3Se_{10}$.

Space group	$P2_1/c$ (#14)
a (Å)	6.6276(6)
b (Å)	13.6010(10)
c (Å)	23.490(4)
$\alpha = \gamma$ (°)	90
β (°)	101.6385(26)
V (Å^3)	2073.9(5)
Radiation	Graphite monochromated Cu Kα (1.54056 Å)
D_{cal} (g/cm^3)	5.3959
2θ range (deg.)	20 - 100
wR_p, R_p	0.04032, 0.03225
GOF	1.063

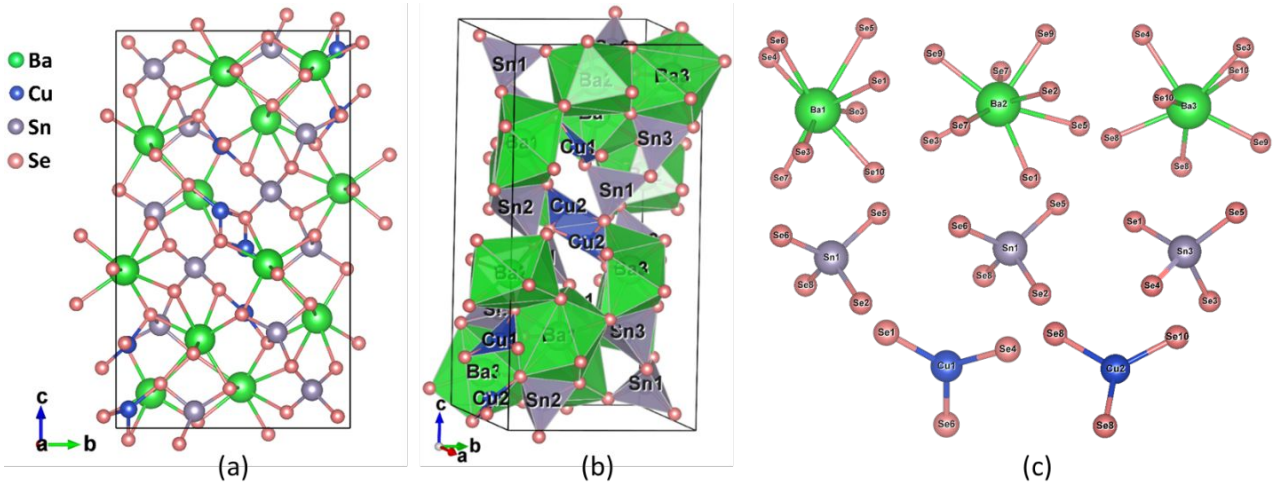

Figure 2. (a) Crystal structure of $Ba_3Cu_2Sn_3Se_{10}$, (b) the structure showing corner sharing and edge sharing polyhedra with cations at their centers, and (c) schematic illustrating the local coordination environment around Ba, Sn and Cu.

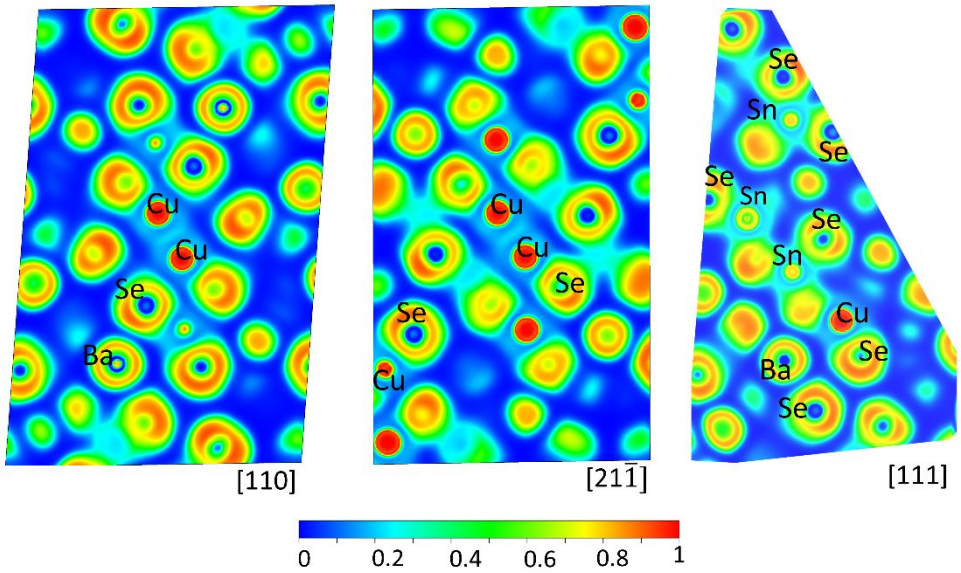

Figure 3. Topological surfaces from calculated ELF along different planes.

ionic/covalent character, as shown in Figure 3. In certain Cu-based crystalline materials, for example those consisting of $CuSe_3$ trigonal environment, strong *p-d* coupling exist and the large U_{iso} for Cu have been correlated to the anti-bonding interactions between filled Cu *d* orbitals and Se *p* orbitals that leads to weaker bonds [16,24,31,32]. The ELF maps (Figure 3) also show such a bonding interaction for the short Cu2-Cu2 distance (2.64 (3) Å) that is consistent with this interpretation [24].

Figure 4 shows DTA data for $Ba_3Cu_2Sn_3Se_{10}$ indicating decomposition into Cu_2SnSe_3 and BaSe at 823 K. Thermal diffusivity was therefore measured well below this temperature. Figure 5 shows the temperature dependence of magnetic susceptibility (χ) and indicates diamagnetic behavior. At temperatures below 30 K, the positive and increasing susceptibility can be attributed to trace magnetic impurities in the elements used for synthesis.

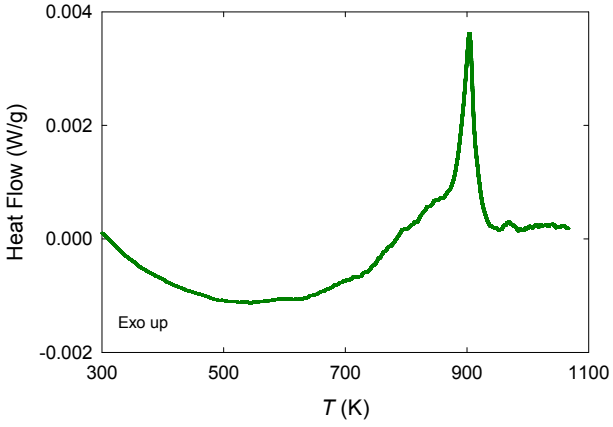

Figure 4. DTA data for $Ba_3Cu_2Sn_3Se_{10}$.

Table 2. Atomic coordinates and equivalent atomic displacement parameters of $Ba_3Cu_2Sn_3Se_{10}$.

atom	site	x	y	z	U_{iso}(Å^2)
Ba1	4*e*	0.67907(11)	0.35884(6)	0.22344(29)	0.023
Ba2	4*e*	0.12646(12)	0.53433(4)	0.10267(3)	0.023
Ba3	4*e*	0.0576(10)	0.14893(5)	0.08726(31)	0.024
Sn1	4*e*	0.36574(13)	0.33777(5)	0.40422(3)	0.013
Sn2	4*e*	0.49824(10)	0.33458(6)	0.0427(29)	0.015
Sn3	4*e*	0.21046(10)	0.18682(5)	0.25937(29)	0.018
Cu1	4*e*	0.6603(19	0.0506(10)	0.2099(5)	0.052
Cu2	4*e*	0.5125(19)	0.0537(9)	0.0474(6)	0.046
Se1	4*e*	0.5863(15)	0.14789(8)	0.28532(5)	0.019
Se2	4*e*	0.34519(16)	0.72943(8)	0.03985(5)	0.017
Se3	4*e*	0.16148(18)	0.33059(9)	0.18786(5)	0.025
Se4	4*e*	0.024(17)	0.03765(8)	0.2137(5)	0.020
Se5	4*e*	0.05447(14)	0.24982(7)	0.34456(5)	0.017
Se6	4*e*	0.57893(17)	0.44023(8)	0.34877(5)	0.017
Se7	4*e*	0.63565(21)	0.48634(7)	0.09931(6)	0.019
Se8	4*e*	0.20278(18)	0.44695(8)	0.47068(5)	0.013
Se9	4*e*	0.11457(17)	0.34927(9)	0.01546(5)	0.022
Se10	4*e*	0.57938(19)	0.1901(7)	0.11185(5)	0.017

Table 3. Selected atomic bond lengths and bond angles of $Ba_3Cu_2Sn_3Se_{10}$.

Bond lengths (Å)		Bond angles (°)	
Ba1-Se3	3.3848(4)	Se3-Ba1-Se1	75.09(7)
Ba1-Se6	3.3349(5)	Se4-Ba1-Se1	126.03(7)
Ba1-Se10	3.4461(4)	Se4-Ba1-Se3	132.87(7)
Ba1-Se1	3.3292(3)	Se4-Ba1-Se6	64.24(7)
Ba1-Se7	3.3546(5)	Se3-Ba1-Se6	83.30(7)
Ba1-Se4	3.28561(19)	Se4-Ba1-Se10	147.18(7)
Ba1-Se3	3.4852(3)	Se3-Ba1-Se10	72.98(7)
Ba1-Se5	3.6915(4)	Se6-Ba1-Se10	148.30(7)
Ba2-Se9	3.2362(3)	Se6-Ba1-Se1	79.25(7)
Ba2-Se7	3.4537(4)	Se4-Ba3-Se9	149.55(7)
Ba2-Se1	3.3033(4)	Se4-Ba3-Se3	75.77(7)
Ba2-Se2	3.4905(3)	Se9-Ba3-Se3	73.96(7)
Ba2-Se3	3.3985(3)	Se4-Ba3-Se8	82.60(7)
Ba2-Se5	3.4877(3)	Se9-Ba3-Se8	124.95(7)
Ba2-Se9	3.3121(4)	Se3-Ba3-Se10	73.03(7)
Ba2-Se7	3.3030(3)	Se8-Ba3-Se10	127.95(7)
Ba3-Se4	3.3806(5)	Se8-Ba3-Se10	75.83(7)
Ba3-Se10	3.4351(4)	Se10-Ba3-Se10	152.98(7)
Ba3-Se3	3.3921(3)	Se5-Sn1-Se8	102.39(9)
Ba3-Se9	3.2663(3)	Se5-Sn1-Se2	116.83(9)
Ba3-Se8	3.3450(5)	Se8-Sn1-Se2	112.77(9)
Ba3-Se10	3.3810(3)	Se5-Sn1-Se6	116.79(9)
Ba3-Se8	3.3807(2)	Se8-Sn1-Se6	110.18(9)
Sn1-Se5	2.54642(18)	Se2-Sn1-Se6	98.26(9)
Sn1-Se8	2.5474(3)	Se9-Sn2-Se2	112.59(9)
Sn1-Se2	2.55974(16)	Se9-Sn2-Se10	107.39(9)
Sn1-Se6	2.52537(18)	Se2-Sn2-Se10	99.06(9)
Sn2-Se9	2.5018(3)	Se9-Sn2-Se7	108.03(9)
Sn2-Se10	2.5371(3)	Se2-Sn2-Se7	121.66(9)
Sn2-Se2	2.5311(3)	Se10-Sn2-Se7	106.79(9)
Sn2-Se7	2.52379(17)	Se4-Sn3-Se3	110.63(9)
Sn3-Se4	2.50188(15)	Se5-Sn3-Se3	103.79(9)
Sn3-Se5	2.5772(4)	Se4-Sn3-Se1	108.34(9)
Sn3-Se3	2.5555(3)	Se5-Sn3-Se1	114.67(9)
Sn3-Se1	2.4988(3)	Se3-Sn3-Se1	108.10(9)
Cu1-Se6	2.405(13)	Se4-Cu1-Se6	121.109(13)
Cu1-Se1	2.341(13)	Se4-Cu1-Se1	112.10(13)
Cu1-Se4	2.401(13)	Se6-Cu1-Se1	124.90(13)
Cu2-Se10	2.379(13)	Se8-Cu2-Se8	115.20(13)
Cu2-Se8	2.484(14)	Se8-Cu2-Se10	120.90(13)
Cu2-Se8	2.443(12)	Se8-Cu2-Se10	119.50(13)

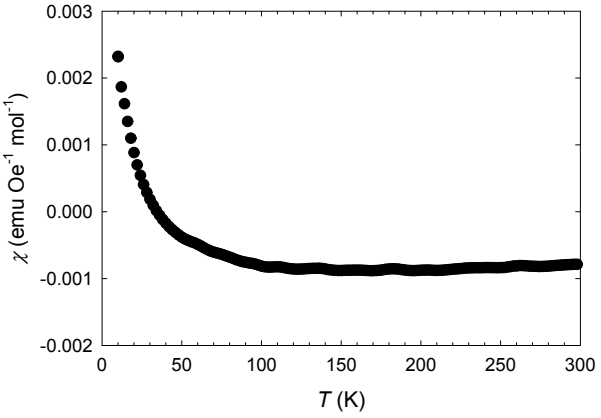

Figure 5. Molar susceptibility (χ) versus temperature for $Ba_3Cu_2Sn_3Se_{10}$ in a magnetic field of 1 T.

Figure 6(a) shows C_p versus T data for $Ba_3Cu_2Sn_3Se_{10}$. The C_p data approaches the Dulong-Petit limit at high temperatures, as shown in the figure, indicating that all the acoustic and optical phonon modes are fully excited at room temperature. The inset shows a fit using the relation $C_p = \alpha T + \beta T^3$, with the first and second terms representing the electronic and the lattice contributions to C_p, respectively [33]. From this fit we obtain $\alpha = 2\ \mathrm{mJ\ mol^{-1}K^{-2}}$ and $\beta = 8\ \mathrm{mJ\ mol^{-1}K^{-4}}$. The α value is small, as expected for this relatively large band gap material [24]. The Debye temperature, θ_D, can be determined using $\theta_D = (12\pi^4 R n_a/5\beta)^{1/3}$, where R is the molar gas constant and n_a is the number atoms per formula unit [33], resulting in a θ_D value of

162 K. The average sound velocity, υ, estimated to be 1666 m/s, can be obtained using the relation $\theta_D = \upsilon(h/k_B)(3n_a N a^d/4\pi M_w)^{1/3}$, where h is Planck's constant, k_B is the Boltzmann constant, N_a is the Avogadro's constant, d is the density, and M_w is the molecular weight. The relatively weak chemical bonding described above can lead to low sound velocities since υ is proportional to $\sqrt{\delta/m}$, where δ is a constant characterizing the bond strength, or stiffness, and m is the atomic mass, consequently suppressing κ [16]. Figure 6(b) shows a maximum in C_p/T^3 versus T indicating deviation from Debye-like behavior that is related to the optic modes with an Einstein temperature, θ_E, of 43 K, the peak found at approximately $1/5$ of θ_E.

Figure 7 show temperature dependent κ data for $Ba_3Cu_2Sn_3Se_{10}$. This quaternary chalcogenide displays ultralow κ values with < 0.5 W m^{-1}K^{-1} in the entire temperature range. For a large bandgap semiconductor, these κ values are associated with the lattice with negligible electronic contribution to κ. The lattice thermal conductivity, κ_l, was shown by Slack to be $\kappa_l = BMV^{1/3}\theta_D^3/n^{2/3}\gamma^2 T$, where $B = 2.43 \cdot 10^{-8}/(1 - 0.514/\gamma + 0.228/\gamma^2)$, M is the average mass of an atom in the crystal (amu), V is the unit cell, n is the number of atoms per primitive cell, γ is the Grüneisen parameter and T is absolute temperature [34–36]. The resulting room temperature γ value is 1.3, a relatively large value indicating relatively large anharmonicity for $Ba_3Cu_2Sn_3Se_{10}$.

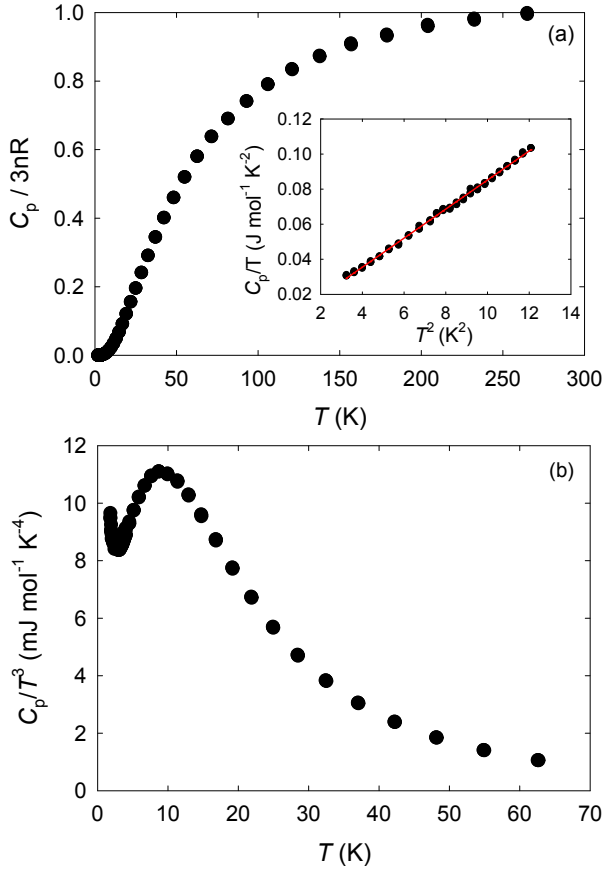

Figure 6. (a) Heat capacity, C_p, data for $Ba_3Cu_2Sn_3Se_{10}$. The data are normalized such that a value of unity represents the Dulong–Petit limit. The inset shows C_p/T versus T^2 data at low temperatures with a solid line fit to the relation $C_p/T = \alpha + \beta T^2$. (b) C_p/T^3 versus T data showing deviation from the Debye model.

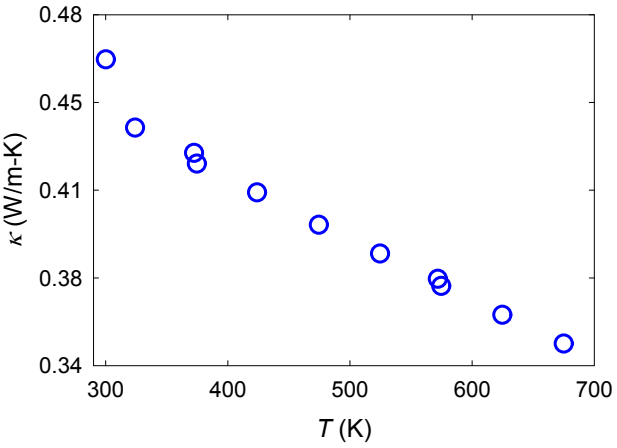

Figure 7. Temperature dependent κ data for $Ba_3Cu_2Sn_3Se_{10}$.

Conclusions

The origins of the ultralow κ values of $Ba_3Cu_2Sn_3Se_{10}$ were identified via structural characterization and analyses of the thermal properties. $Ba_3Cu_2Sn_3Se_{10}$ forms in monoclinic crystal structure with 72 atoms per unit cell consisting of high local coordination of cation-centered polyhedra formed by selenium atoms. Cu atoms have relatively large U_{iso}, as compared to the other constituent atoms, indicating relatively weak Cu-Se bonding. The presence of bonding between Cu2 atoms is reflected in the ELF analyses. The very low κ for this material originates from low sound velocity, low-frequency Einstein optical modes, and intrinsic lattice anharmonicity in addition to a large unit cell.

Conflicts of interest

There are no conflicts to declare.

Acknowledgements

This work was supported, in part, by the National Science Foundation, Grant No. DMR-1748188. H.W. acknowledges support of the U.S. Department of Energy, Office of Energy Efficiency and Renewable Energy, Vehicle Technologies Office, Powertrain Materials Core Program. Oak Ridge National Laboratory is managed by UT-Battelle LLC under contract DE-AC05000OR22725.

Notes and references

1 A. Abudurusuli, J. Li and S. Pan, *Dalt. Trans.*, 2021, **50**, 3155–3160.

2 K. Wu and S. Pan, *Coord. Chem. Rev.*, 2018, **377**, 191–208.

3 M. Y. Li, Z. Ma, B. Li, X. T. Wu, H. Lin and Q. L. Zhu, *Chem. Mater.*, 2020, **32**, 4331–4339.

4 W. Xing, N. Wang, A. K. Iyer, W. Yin, Z. Lin, J. Yao, B. Kang and A. Mar, *J. Alloys Compd.*, 2020, **846**, 156398.

5 K. Pal, P. Singh, A. Bhaduri and K. B. Thapa, *Sol. Energy Mater. Sol. Cells*, 2019, **196**, 138–156.

6 M. Ravindiran and C. Praveenkumar, *Renew. Sustain. Energy Rev.*, 2018, **94**, 317–329.

7 P. Kush and S. Deka, *ChemNanoMat*, 2019, **5**, 373–402.

8 M. Sahu, V. R. Minnam Reddy, C. Park and P. Sharma, *Sol. Energy*, 2021, **230**, 13–58.

9 K. Pal, Y. Xia, J. Shen, J. He, Y. Luo, M. G. Kanatzidis and C. Wolverton, *npj Comput. Mater. 2021 71*, 2021, **7**, 1–13.

10 T. R. Wei, Y. Qin, T. Deng, Q. Song, B. Jiang, R. Liu, P. Qiu, X. Shi and L. Chen, *Sci. China Mater. 2018 621*, 2018, **62**, 8–24.

11 P. Qiu, X. Shi and L. Chen, *Energy Storage Mater.*, 2016, **3**, 85–97.

12 K. Wei, L. Beauchemin, H. Wang, W. D. Porter, J. Martin and G. S. Nolas, *J. Alloys Compd.*, 2015, **650**, 844–847.

13 Y. Dong, H. Wang and G. S. Nolas, *Phys. status solidi - Rapid Res. Lett.*, 2014, **8**, 61–64.

14 D. R. Clarke and C. G. Levi, *Annu. Rev. Mater. Res.*, 2003, **33**, 383–417.

15 R. Darolia, *Int. Mater. Rev.*, 2013, **58**, 315–348.

16 J. He, Y. Xia, W. Lin, K. Pal, Y. Zhu, M. G. Kanatzidis, C. Wolverton, J. He, Y. Xia, K. Pal, Y. Zhu, C. Wolverton, W. Lin and M. G. Kanatzidis, *Adv. Funct. Mater.*, 2021, 2108532.

17 Y. Dong, A. R. Khabibullin, K. Wei, J. R. Salvador, G. S. Nolas and L. M. Woods, ChemPhysChem, 2015, **16**, 3264–3270.

18 C. Bourgès, Y. Bouyrie, A. R. Supka, R. Al Rahal Al Orabi, P. Lemoine, O. I. Lebedev, M. Ohta, K. Suekuni, V. Nassif, V. Hardy, R. Daou, Y. Miyazaki, M. Fornari and E. Guilmeau, J. Am. Chem. Soc., 2018, **140**, 2186–2195.

19 W. D. C. B. Gunatilleke, A. F. May, H. Wang and G. S. Nolas, *Appl. Phys. Lett.*, 2020, **117**, 092101.

20 W. D. C. B. Gunatilleke, N. Alzahrani, A. F. May, H. Wang and G. S. Nolas, *Phys. status solidi – Rapid Res. Lett.*, 2020, **14**, 2000363.

21 W. D. C. B. Gunatilleke, R. Juneja, O. P. Ojo, A. F. May, H. Wang, L. Lindsay and G. S. Nolas, *Phys. Rev. Mater.*, 2021, **5**, 085002.

22 T. Mori, J. Martin and G. Nolas, *J. Appl. Phys.*, 2007, **102**, 073510.

23 M. Beekman and G. S. Nolas, *Phys. B Condens. Matter*, 2006, **383**, 111–114.

24 Abdeljalil Assoud, A. Navid Soheilnia and H. Kleinke, *Chem. Mater.*, 2005, **17**, 2255–2261.

25 B. H. Toby and R. B. Von Dreele, *J. Appl. Crystallogr.*, 2013, **46**, 544–549.

26 P. Giannozzi, S. Baroni, N. Bonini, M. Calandra, R. Car, C. Cavazzoni, D. Ceresoli, G. L. Chiarotti, M. Cococcioni, I. Dabo, A. Dal Corso, S. De Gironcoli, S. Fabris, G. Fratesi, R. Gebauer, U. Gerstmann, C. Gougoussis, A. Kokalj, M. Lazzeri, L. Martin-Samos, N. Marzari, F. Mauri, R. Mazzarello, S. Paolini, A. Pasquarello, L. Paulatto, C. Sbraccia, S. Scandolo, G. Sclauzero, A. P. Seitsonen, A. Smogunov, P. Umari and R. M. Wentzcovitch, *J. Phys. Condens. Matter*, 2009, **21**, 395502.

27 J. P. Perdew, K. Burke and M. Ernzerhof, *Phys. Rev. Lett.*, 1997, **78**, 1396.

28 J. P. Perdew, M. Ernzerhof and K. Burke, *J. Chem. Phys.*, 1998, **105**, 9982.

29 P. E. Blöchl, O. Jepsen and O. K. Andersen, *Phys. Rev. B*, 1994, **49**, 16223.

30 K. Momma and F. Izumi, *J. Appl. Crystallogr.*, 2008, **41**, 653–658.

31 S. H. Wei and A. Zunger, *Phys. Rev. B*, 1988, **37**, 8958–8981.

32 J. E. Jaffe and A. Zunger, *Phys. Rev. B*, 1984, **29**, 1882.

33 C. Kittel, *Introduction to solid state physics.*, John Wiley & Sons, Inc., Fifth edit., 1976.

34 D. Morelli and G. Slack, *High lattice thermal conductivity solids. In High thermal conductivity materials*, Springer, New York, 2006.

35 G. A. Slack, Solid State Phys., 1979, 34, 1–71.

36 C. L. Julian, *Phys. Rev.*, 1965, **137**, A128.